

This work was written as part of one of the author's official duties as an Employee of the United States Government and is therefore a work of the United States Government. In accordance with 17 U.S.C. 105, no copyright protection is available for such works under U.S. Law.

Public Domain Mark 1.0

<https://creativecommons.org/publicdomain/mark/1.0/>

Access to this work was provided by the University of Maryland, Baltimore County (UMBC) ScholarWorks@UMBC digital repository on the Maryland Shared Open Access (MD-SOAR) platform.

Please provide feedback

Please support the ScholarWorks@UMBC repository by emailing scholarworks-group@umbc.edu and telling us what having access to this work means to you and why it's important to you. Thank you.

All-sky Medium Energy Gamma-ray Observatory eXplorer mission concept

Regina Caputo^{a,*}, Marco Ajello^b, Carolyn A. Kierans^a,
Jeremy S. Perkins^a, Judith L. Racusin^a, Luca Baldini^c,
Matthew G. Baring^d, Elisabetta Bissaldi^{e,f}, Eric Burns^g,
Nicholas Cannady^{a,h,i}, Eric Charles^j, Rui M. Curado da Silva^k,
Ke Fang^l, Henrike Fleischhack^{a,h,m}, Chris Fryerⁿ, Yasushi Fukazawa^o,
J. Eric Grove^p, Dieter Hartmann^b, Eric J. Howell^q, Manoj Jadhav^r,
Christopher M. Karwin^b, Daniel Kocevski^s, Naoko Kurahashi^t,
Luca Latronico^u, Tiffany R. Lewis^v, Richard Leys^w, Amy Lien^x,
Lea Marcotulli^y, Israel Martinez-Castellanos^{a,h,z}, Mario Nicola Mazzotta^f,
Julie McEnery^a, Jessica Metcalfe^r, Kohta Murase^{aa,ab}, Michela Negro^{a,h,i},
Lucas Parker^{ac}, Bernard Philips^p, Chanda Prescod-Weinstein^{ad},
Soebur Razzaque^{ae,af}, Peter S. Shawhan^z, Yong Sheng^b, Tom A. Shutt^{ag,ah},
Daniel Shy^{ai}, Clio Sleator^p, Amanda L. Steinhebel^v, Nicolas Striebig^{b,w},
Yusuke Suda^o, Donggeun Tak^{aj}, Hiro Tajima^{ak}, Janeth Valverde^{a,h,i},
Tonia M. Venters^a, Zorawar Wadiasingh^{a,h,al}, Richard S. Woolf^p,
Eric A. Wulf^p, Haocheng Zhang^v and Andreas Zoglauer^{am}

^aNASA Goddard Space Flight Center, Greenbelt, Maryland, United States

^bClemson University, Department of Physics and Astronomy, Clemson, South Carolina,
United States

^cUniversità di Pisa and Istituto Nazionale di Fisica Nucleare, Pisa, Italy

^dRice University, Department of Physics and Astronomy, Houston, Texas, United States

^eDipartimento Interateneo di Fisica dell'Università e del Politecnico di Bari, Bari, Italy

^fIstituto Nazionale di Fisica Nucleare, Sezione di Bari, Bari, Italy

^gLouisiana State University, Department of Physics and Astronomy, Baton Rouge,
Louisiana, United States

^hCenter for Research and Exploration in Space Science and Technology, NASA/GSFC,
Greenbelt, Maryland, United States

ⁱUniversity of Maryland, Baltimore, Maryland, United States

^jStanford University, Kavli Institute for Particle Astrophysics and Cosmology,

W. W. Hansen Experimental Physics Laboratory, Department of Physics and

SLAC National Accelerator Laboratory, Stanford, California, United States

^kUniversidade de Coimbra, Laboratório de Instrumentação e Física Experimental de Partículas,
Departamento de Física, Coimbra, Portugal

^lUniversity of Wisconsin–Madison, Department of Physics, Madison,
Wisconsin, United States

^mCatholic University of America, Washington, DC, United States

ⁿCenter for Theoretical Astrophysics, Los Alamos National Laboratory, Los Alamos,
New Mexico, United States

^oHiroshima University, Department of Physics, Hiroshima, Japan

^pU.S. Naval Research Laboratory, Space Science Division, Washington, DC, United States

^qOzGrav, University of Western Australia, Crawley, Western Australia, Australia

^rArgonne National Laboratory, Lemont, Illinois, United States

^sNASA Marshall Space Flight Center, Huntsville, Alabama, United States

^tDrexel University, Department of Physics, Philadelphia, Pennsylvania, United States

^uINFN, Sezione di Torino, Torino, Italy

^vNASA Postdoctoral Fellow, NASA Goddard Space Flight Center, Greenbelt, Maryland,
United States

^wKarlsruhe Institute of Technology (KIT-ADL) – Hermann-von-Helmholtz-Platz,
Karlsruhe, Germany

^xUniversity of Tampa, Department of Chemistry, Biochemistry, and Physics, Tampa, Florida, United States

^yYale University, Department of Physics, New Haven, Connecticut, United States

^zUniversity of Maryland, Department of Physics, College Park, Maryland, United States

^{aa}The Pennsylvania State University, Institute for Gravitation and the Cosmos, Department of Physics, Department of Astronomy and Astrophysics, University Park, Pennsylvania, United States

^{ab}Yukawa Institute for Theoretical Physics, Center for Gravitational Physics, Kyoto, Japan

^{ac}Los Alamos National Laboratory, Los Alamos, New Mexico, United States

^{ad}University of New Hampshire, Department of Physics and Astronomy, Durham, New Hampshire, United States

^{ae}University of Johannesburg, Centre for Astro-Particle Physics, Department of Physics, Auckland Park, South Africa

^{af}The George Washington University, Department of Physics, Washington, DC, United States

^{ag}SLAC National Accelerator Laboratory, Menlo Park, California, United States

^{ah}Stanford University, Kavli Institute for Particle Astrophysics and Cosmology, Stanford, California, United States

^{ai}National Research Council, Naval Research Laboratory, Washington, DC, United States

^{aj}Deutsches Elektronen-Synchrotron (DESY), Zeuthen, Germany

^{ak}Nagoya University, Institute for Space–Earth Environmental Research,

Kobayashi-Maskawa Institute for the Origin of Particles and the Universe, Nagoya, Japan

^{al}University of Maryland, Department of Astronomy, College Park, Maryland, United States

^{am}University of California at Berkeley, Space Sciences Laboratory, Berkeley, California, United States

Abstract. The All-sky Medium Energy Gamma-ray Observatory eXplorer (AMEGO-X) is designed to identify and characterize gamma rays from extreme explosions and accelerators. The main science themes include supermassive black holes and their connections to neutrinos and cosmic rays; binary neutron star mergers and the relativistic jets they produce; cosmic ray particle acceleration sources including galactic supernovae; continuous monitoring of other astrophysical events and sources over the full sky in this important energy range. AMEGO-X will probe the medium energy gamma-ray band using a single instrument with sensitivity up to an order of magnitude greater than previous telescopes in the energy range 100 keV to 1 GeV that can be only realized in space. During its 3-year baseline mission, AMEGO-X will observe nearly the entire sky every two orbits, building up a sensitive all-sky map of gamma-ray sources and emissions. AMEGO-X was submitted in the recent 2021 NASA MIDEX announcement of opportunity. © 2022 Society of Photo-Optical Instrumentation Engineers (SPIE) [DOI: [10.1117/1.JATIS.8.4.044003](https://doi.org/10.1117/1.JATIS.8.4.044003)]

Keywords: multimessenger; gamma-ray telescope; high-energy astrophysics; gamma-ray mission.

Paper 22068G received Jun. 27, 2022; accepted for publication Oct. 5, 2022; published online Oct. 28, 2022.

1 Introduction

Multimessenger astrophysics is one of the most exciting and rapidly advancing fields of science, providing unparalleled access to extreme processes that sculpt the universe. Gamma-ray observations have been central to the advent of the multimessenger initiative and will continue to be so as the field matures. As a priority theme of the Astro2020 Decadal Survey report,¹ the science of New Messengers New Physics is poised to revolutionize our understanding of the extreme universe. Data from NASA's *Fermi* mission has demonstrated that many of the extreme processes

*Address all correspondence to Regina Caputo, regina.caputo@nasa.gov

that produce gravitational waves and neutrinos and accelerate cosmic rays also produce gamma rays. In other words, *multimessenger sources are gamma-ray sources*. These sources are, however, brightest in the under-explored MeV band. We have developed a mission and submitted a proposal to the 2021 NASA astrophysics medium explorer (MIDEX) announcement of opportunity² to observe these critical energies and fully capitalize on this exciting new era of multimessenger astrophysics.

The All-sky Medium Energy Gamma-ray Observatory eXplorer (AMEGO-X) is a wide-field survey telescope designed to discover and characterize gamma-ray emission from multimessenger sources using imaging, spectroscopy, and polarization. During its 3-year baseline mission, AMEGO-X will observe in the critical 100 keV to 1 GeV energy band over nearly the entire sky every two orbits, building up a sensitive all-sky map of gamma-ray sources and diffuse emission. It will also access $>50\%$ (<10 MeV) and $>20\%$ (>10 MeV) of the sky instantaneously, maximizing transient detections and rapid alerts, which will be openly distributed to the astrophysics communities. AMEGO-X will deliver breakthrough discoveries in a MIDEX class mission in areas highlighted as the highest scientific priority for explorer-scale missions in the Astro2020 Decadal Survey Report: multimessenger astrophysics and time-domain astronomy. AMEGO-X complements the recently selected the COmpton Spectrometer Imager (COSI) small explorer mission,³ which has excellent energy resolution in the 0.2 to 5 MeV band to probe the origins of galactic positrons and uncover sites of nucleosynthesis. AMEGO-X will provide a leap ($\times 10 - 50$) in continuum sensitivity, similar to Fermi/LAT at higher energies, in the long sought-after MeV gamma-ray gap. The AMEGO-X mission employs a single instrument with subsystems delivered by Argonne National Laboratory, the Naval Research Laboratory and NASA Goddard Space Flight Center and has partnered with Lockheed Martin Space for the high-heritage spacecraft.

2 Science

After a long hiatus from the first multimessenger event SN 1987A,⁴ which was discovered in optical and neutrinos, a new era of multimessenger astrophysics was heralded in 2017 when the electromagnetic counterparts to sources of both neutrinos^{5,6} and gravitational waves^{7,8} were observed for the first time. The AMEGO-X mission has three overarching goals which tie together the extreme explosions and extreme accelerators which produce all the cosmic messengers: supermassive black holes, neutron stars and their mergers, and the remnants of galactic supernovae. The following section will expand upon these overarching science goals.

2.1 Supermassive Black Holes and their Connections to Neutrinos and Cosmic Rays

Active galactic nuclei (AGN), accreting supermassive black holes at the centers of galaxies, provide extreme conditions that are conducive to the particle acceleration that is inferred from observations of nonthermal X-rays and gamma rays. This can take place near the black hole (core) and/or in the relativistic jets that 10% of AGN display. Those AGN with a relativistic jet aligned along our line of sight are called blazars⁹ and are the most powerful persistent sources of electromagnetic radiation in the universe. Blazars are widely believed to be sites for rapid acceleration of electrons in their jets to near the speed of light because their low energy spectra are consistent with electron synchrotron emission and optical polarization measurements confirm this.¹⁰ They are also powerful enough to accelerate protons and may be responsible for the generation of ultra-high energy cosmic rays (UHECRs). The detection of the high-energy neutrino, IC-170922A, by the IceCube Neutrino Observatory (IceCube) coincident with the brightly flaring gamma-ray blazar, TXS 0506+056, marked a milestone in multimessenger astrophysics.^{5,6} It established observationally that at least some blazars accelerate protons: neutrinos are a unique signature of proton acceleration and production because they cannot be produced in purely leptonic sources, instead being produced as decay products of pions and muons in photohadronic collisions. However, the picture is far from complete, as it is not clear which among jetted or nonjetted AGN can accelerate protons. The “smoking gun” signatures of proton

acceleration in AGN are either the coincident detection of high-energy PeV neutrinos and medium-energy (MeV) gamma rays in a particular AGN, and/or detection of polarized emission¹¹ in the MeV band. AMEGO-X, with its sensitive all-sky monitoring, will detect over 400 blazars, which is determined considering the log N - log S distributions of Swift/BAT and Fermi/LAT blazars.^{12–14} Using the second FAVA catalog,¹⁵ it will also detect around 150 blazar flares/year, and for the brightest of these also measure the polarization fraction for more than 10 blazar flares/year, which is the sensitivity to measure polarization within a week. This will allow us to answer long-standing questions about the source of cosmic neutrinos, extragalactic cosmic rays, while also providing critical gamma-ray capabilities complementary to upgraded neutrino observatories in the era of multimessenger astrophysics.

2.1.1 Blazars and their flares

Relativistic jets produce gamma rays through the interactions of the particles they accelerate. In leptonic models, accelerated electrons produce all observed gamma rays, principally via synchrotron and inverse Compton emission. In hadronic models, accelerated protons produce gamma rays through proton-synchrotron radiation¹⁶ or via synchrotron radiation from secondary particles generated by proton interactions with jet photons (via e.g., photo-pion production), the latter of which also produces neutrinos.¹⁷ For most flare data from currently operating observatories, it is not possible to determine which scenario better describes the data – both hadronic and leptonic models are consistent with observed blazar spectra.^{10,18,19} Some hadronic emission-dominated models predict that significant high-energy (GeV) gamma rays interact with jet photons (effectively being absorbed) and are reprocessed into the medium-energy gamma-ray band where they can finally escape the jet. By monitoring the entire medium-energy gamma-ray (100 keV to 1 GeV) sky every 3 h, AMEGO-X will observe in real-time the potential sources of IceCube neutrinos and correlate the timing between gamma-ray and neutrino flares. Figure 1(a) shows a simulated AMEGO-X light curve for which the first and second neutrino flare of TXS 0506+056 could have been detected, since gamma rays and neutrinos are produced via the same processes.²¹ While hadronic models link neutrinos with gamma rays in the AMEGO-X band, the same cannot be said for higher energies. The brightest neutrino events may not be detected by higher-energy gamma-ray telescopes, such as the Fermi/LAT, because the radiation fields required for efficient neutrino production make the source opaque to high-energy gamma rays (e.g., Refs. 19 and 22). Figure 1(b) shows that during the 2014 to 2015 TXS 0506+056 orphan neutrino flare, AMEGO-X may have detected a significant MeV flare if the emission was from hadronic interactions within the AGN corona.

By monitoring nearly the full sky every 3 h, AMEGO-X will detect ~ 150 blazar flares/year, the most promising counterparts to IceCube high-energy neutrinos which are released through

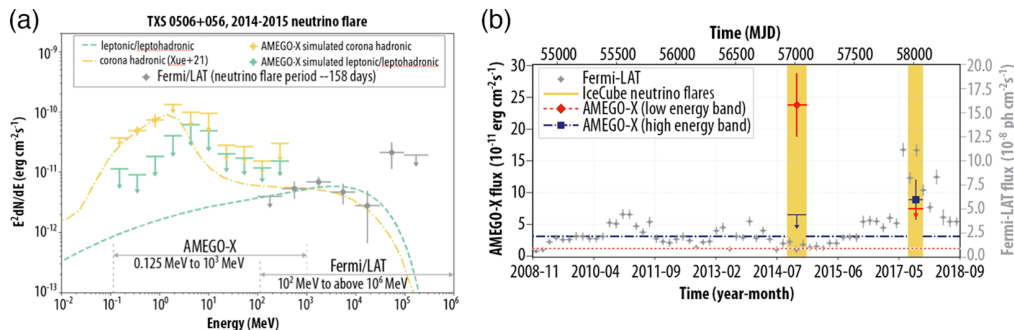


Fig. 1 Simulated AMEGO-X SED for the 2014 flare of TXS 0506+056. The green dashed line is representative of leptonic and leptohadronic models, while the yellow dot-dashed line is the two-zone hadronic model where one of the zones is from the AGN corona from Ref. 20. (a) The gray data points are measurements from Fermi/LAT. Light-curve of TXS 0506+056. The gray data points are measurements from Fermi/LAT. (b) The yellow band shows the times of the IceCube neutrino flares. The green data points are simulated AMEGO-X detection of the MeV emission during those flares. See Ref. 21 for more details.

real-time alerts.²³ AMEGO-X will provide an all-sky catalog of >400 MeV peaked blazars for neutrino searches.¹² These are the most powerful blazars, whose maximum energy output is in the AMEGO-X band. In blazars, the number of high-energy neutrinos correlates with the total 1 keV to 1 PeV flux, which is well approximated by the 100 keV to 1 GeV flux, since this is the band where blazars release the most energy.²⁴ The number of expected IceCube-AMEGO-X coincident detections (over 3 years) for the baseline and threshold missions is $7.7(\pm 2.5)$ and $6(\pm 2)$, respectively (Sec. 3), with the brightest sources expected to emit more than one high-energy neutrino within the 3 years. This has been computed from the number of expected neutrinos from each source following:²⁴

$$N_{\nu} = N_{\nu, \max}(f_{\text{blazar}}) * f_{\text{corr}} * 3/4, \quad (1)$$

where $N_{\nu, \max}$ is the maximum number of expected neutrinos (in 4 years) for a given blazar with an average flux f_{blazar} . $f_{\text{corr}} = 0.0089$ is a correction that takes into account realistic blazar spectra, neutrino flavors and different classes of blazars (conservative estimate²⁴). The factor $3/4$ accounts for the different integration time (4 years in Ref. 24) compared with the expected 3-year duration of the AMEGO-X survey. Moreover, the AMEGO-X survey of the most powerful blazars will also be crucial to determine their contribution to the IceCube diffuse astrophysical neutrino flux, the origins of which remain a mystery.²⁵

2.1.2 Polarization measurements of jetted active galactic nuclei

Multiwavelength spectral observations alone cannot yet distinguish if blazars accelerate only leptons or leptons and hadrons (e.g., Refs. 26 and 27). In blazar models for which at least part of the gamma-ray emission is from proton acceleration, the polarization signature is prominent in the medium-energy gamma-ray band.¹¹ This is because the relativistic Compton scattering dominates the high-energy emission in leptonic models and produces a much lower fraction of polarization than the proton and cascade synchrotron emission in the hadronic model.²⁸ AMEGO-X polarization measurements of blazars will provide an independent constraint on proton acceleration in AGN complementary to coincident neutrino detection.²⁹ While IXPE³⁰ can detect X-ray polarization from blazar jets, this polarization probes the acceleration mechanism of the relativistic electrons, which produce the emission in the X-ray band. On the other hand, AMEGO-X will explore hadronic signatures via MeV polarimetry for blazars, unambiguously identifying proton acceleration and neutrino production in blazar jets, which are essential to multimessenger astronomy. Blazar spectral models have shown that many BL Lacertae objects (BL Lacs), in particular intermediate-synchrotron-peaked and high-synchrotron-peaked BL Lacs, have a significant or even dominating contribution from the primary electron synchrotron component.³¹ In these cases, IXPE detected polarization would indicate leptonic, not hadronic, interactions in the X-ray band. Furthermore, MeV polarimetry can uniquely probe proton synchrotron emission in blazar jets. As shown in Fig. 2, AMEGO-X can clearly distinguish the model with leptonic Compton scattering and hadronic cascades (hybrid model) versus the fully hadronic models with proton synchrotron emission (hadronic model), which is not possible at lower energies. This is because these sources, mostly flat-spectrum radio quasars, are too faint at X-ray energies for IXPE to distinguish polarization degrees of a few percentages (like those, e.g., in Fig. 2). Discovering fully hadronic sources (those with proton synchrotron emission) will allow AMEGO-X to unveil the origin of ultra-high-energy cosmic rays, something not possible without observations in the MeV gamma-ray regime.

AMEGO-X will measure the gamma-ray polarization fraction as low as 10% for at least 10 bright blazar flares per year (e.g., from 3C 279, PKS 1510-089) and two nearby persistent blazars (3C 273 and 3C 454.3), determining whether AGN jets accelerate high-energy cosmic-ray (CR) protons for the first time at these energies. A measured polarization fraction $>30\%$ will allow AMEGO-X to independently establish blazars as extragalactic CR accelerators.^{11,28}

2.1.3 The AGN core

IceCube has recently identified NGC 1068, a nearby AGN lacking a relativistic jet, as a potential neutrino source;³² this provides evidence that AGN without a jet may also accelerate protons and

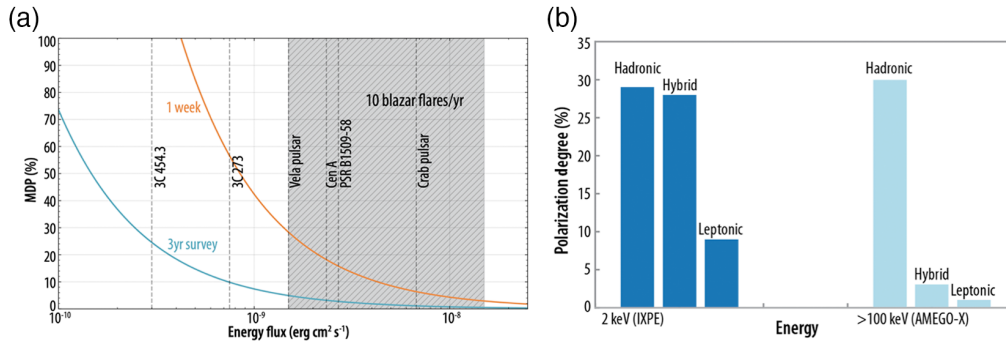


Fig. 2 (a) With a minimum detectable polarization of 25% for faint sources during the 3 year survey, AMEGO-X will be able to discover blazars whose high-energy emission is of hadronic nature.¹¹ (b) AMEGO-X observations complement IXPE's because polarization at different energies probes different blazar populations, radiation processes and possibly even different acceleration mechanisms. Polarization fractions for blazars with a fully hadronic, leptonic or hybrid (mix of leptonic and hadronic) emission models in the IXPE and AMEGO-X band.

produce neutrinos. Within the immediate vicinity of the supermassive black hole (AGN core), accretion cultivates extreme environments conducive to particle acceleration. Clouds of hot thermal electrons exist above the disk in the corona and have a thermal energy distribution.³³ However, there is recent evidence of accelerated (nonthermal) electrons that may produce MeV emission via inverse Compton scattering of disk photons.^{34,35} Similarly, protons can be accelerated near the disk.³⁶ AMEGO-X's continuum sensitivity will allow the detection of these thermal and nonthermal leptonic and/or hadronic components (Fig. 3 for NGC 1068) in off-axis jetted (e.g., Cen A, M87) and nonjetted (e.g., NGC 1068, NGC 3516, NGC 4258) AGN.

2.2 Binary Neutron Star Mergers and their Jets

In-spiraling and merging binary neutron stars (BNSs) emit gravitational waves (GWs), and ripples in spacetime that can be detected by the worldwide GW network.³⁷ After the merger, particles are accelerated in narrowly collimated relativistic jets launched along the rotational axis. When these jets point toward Earth, we observe a bright flash of gamma rays, a short gamma-ray burst (SGRB), in the tens of keV to few MeV energy bands. GW170817/GRB170817A was the first BNS merger that jointly detected both with gamma rays and GWs, informing telescopes around the world to follow up on the event.^{7,8,38} Despite the wealth of information gained through

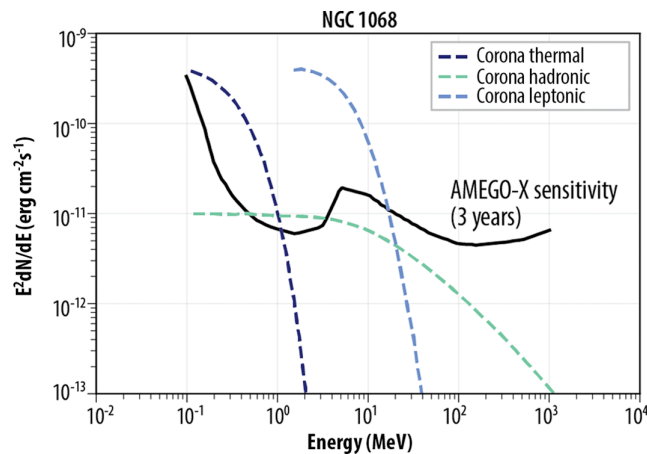


Fig. 3 Expected emission from the AGN corona of NGC 1068. The blue dashed line shows the corona thermal emission, the light blue and green dashed lines show the nonthermal leptonic and hadronic components, respectively.³⁶ The solid black line shows the AMEGO-X sensitivity assuming a 3 year mission.

multiwavelength observations of this event and the associated radioactively powered isotropic kilonova emission³⁹ and the off-axis afterglow, fundamental questions regarding the nature of BNS mergers remain. For example, a higher-mass BNS merger, GW 190425,⁴⁰ had no associated SGRB detected by current missions, which could be due to a different merger remnant or to an off-axis jet that was pointed away from Earth. The large 90% localization region of 10,200 deg² was not fully covered by current instruments. Swift/BAT reported that 45.73% of the localization probability region was outside the field-of-view⁴¹ and only 55.6% of the probability region was viewable by Fermi/GBM.⁴² A population of joint observations of BNS mergers, in GW and gamma rays, will address these questions, enabling the science that is impossible to perform independently or at other wavelengths. The medium-energy gamma-ray band, where SGRBs are the brightest, provides unique insight into the physics of BNS mergers making AMEGO-X ideally positioned to provide a new, comprehensive view of this population.

2.2.1 Model-dependent statistical fractions and structure of GRB jets

A BNS merger can produce one of four possible remnants: a stable NS, a long-lived massive NS supported by its fast rigid-body-like rotation, a short-lived massive NS supported by internal differential rotation, or prompt black hole formation. Each outcome leads to different predictions for the presence or absence of a relativistic jet, as well as the characteristic delay between the merger event and the formation and launching of the jet.⁴³ For events detected jointly (estimates are later in the section), the GW data provide information on NS masses, spins, and distances, but AMEGO-X observations are required to probe the nature of the merger remnant and the structure of the jet. Joint observations of ten BNS mergers can constrain the maximum NS mass to $\sim 1\%$ precision, improving the current constraints by nearly an order of magnitude.⁴⁴ Typical AMEGO-X on-board SGRB localizations will have a factor of 400 smaller localization uncertainties (90% confidence regions) compared with Fermi/GBM,^{45,46} which will dramatically decrease the time needed to search for and precisely localize the SGRB afterglow or kilonova emission via X-ray, optical, and radio follow-up. This increases the fraction of events with early broadband observations including spectroscopy and an opportunity to characterize the early evolution of these objects. The AMEGO-X $\lesssim 10$ deg² 90% confidence region [Fig. 4(a)] is well matched to the fields of view (FOVs) of current facilities like the gravitational wave optical transient observer (GOTO)⁵⁰ and the Zwicky transient facility (ZTF),⁵¹ and the future Vera C. Rubin Telescope.⁵² Those multiwavelength observations will provide insights into the host galaxy including redshift, source dynamics, and kilonova emission, complementing the

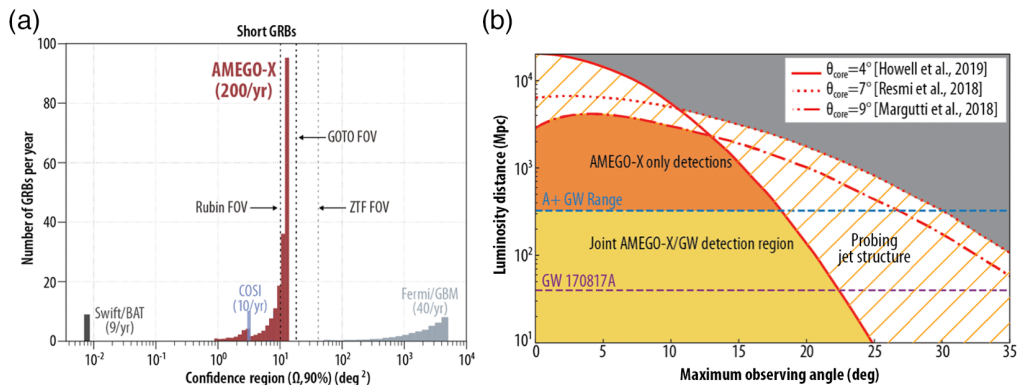


Fig. 4 (a) Comparison of the detection rate vs. localization accuracy for AMEGO-X, Swift/BAT, Fermi/GBM and COSI. (b) The distance by AMEGO-X, versus jet observing angle for SGRBs (right). The solid, dot-dashed and dotted lines show jet structure models (from respectively Refs. 47–49) compatible with the observations of the GRB170817A. An event falling within the yellow shaded area will be detected both by AMEGO-X and the GW network. Observations or nonobservations of events that lie below the blue dashed line and within the hatched area will indicate the extent of the GRB jet opening angle. Events in the orange area are detectable by AMEGO-X, but outside of the range of the GW network.

AMEGO-X jet energetics and emission mechanisms. AMEGO-X's rapid SGRB localizations enable the >2000 observers (subscribers to the gamma-ray coordinates network, GCN) to quickly search and identify the potential counterparts. This population would inform not only the uniqueness of GW170817 but also the nature of the progenitors and remnant objects from compact binary mergers.

Notably under-luminous compared with previously detected SGRBs,^{7,38} the energetic core of GRB170817A's relativistic jet was not completely aligned with our line of sight⁵³ ($\sim 20^\circ$ deg -25° deg off-axis). The observed emission supports the structured jet scenario, in which the jet interacts with the ejecta from the BNS merger resulting in a narrowly collimated energetic jet core with a gradual decrease in flux and Lorentz factor away from the core.^{54,55} Under this structured jet scenario, the observed luminosity has a strong dependence on the viewing angle with respect to the jet axis and can be parameterized by a Gaussian function defined by the opening angle (θ_{core}) and luminosity of the jet [Fig. 4(b)] and only nearby SGRBs can be detected at wider viewing angles. Most BNS mergers are expected near the GW detectability horizon (or the maximum distance the GW network is sensitive) where the volumetric rate will be higher. This distance-viewing angle phase space [Fig. 4(b)] provides a means to directly probe the structured jet profile. Here, we note that AMEGO-X detection and nondetection of GW-detected BNS mergers will set fundamental constraints on the structure of the jet.

Of the 80^{+180}_{-50} /yr GW-detected BNS mergers that will fall within AMEGO-X's FOV in the late 2020s (all orientations),⁵⁶ $\sim 40\%$ (30^{+68}_{-19} /yr) will have jets oriented within 30° deg with a 90% CL. This assumes 80% duty cycle per GW detector (i.e., 64% for both LIGO detectors) and that AMEGO-X observes 50% of the sky instantaneously for GRBs. Among those, the fraction of detected SGRBs will strongly constrain the jet structure. For example, for the narrowest and widest jet models of Fig. 4 (compatible with GRB170817A) one expects an average $\sim 10\%$ (3^{+5}_{-2} /yr) and $\sim 25\%$ (6^{+10}_{-4} /yr) joint GW-SGRB detections, respectively.⁴⁷ Knowledge of the GW distances will allow AMEGO-X observations (both detections and nondetections) to place constraints on different jet structure models and their parameterization such as the parameters of the Gaussian structured jet, or more complicated models such as two-component structured jet (Fig. 4).⁴⁷ Although not the favored scenario for GRB170817A, a cocoon shock breakout can produce SGRBs over a much wider range of viewing angles, despite carrying only a fraction of the energy of the jet.⁵⁷ In all jointly observed GW-SGRB events, AMEGO-X will be able to detect or rule out the soft (<200 keV) emission associated with shock breakout. This population of BNS mergers will constrain the jet parameters providing insights into the formation of relativistic outflows.

Beyond BNS mergers, AMEGO-X will also provide observations of more than a hundred GW-detected neutron star black hole (NSBH) mergers during its mission lifetime. These observations will determine if NSBH mergers emit gamma rays.⁵⁸ Without measurements in the medium-energy gamma-ray band, a critical piece for understanding the remnant and potential jet production of the GW-detected NSBH mergers will be missing.

Recent very high-energy (VHE) detections of GRB afterglows have accentuated the issue of whether gamma-ray afterglows violate the maximum synchrotron energy or if a synchrotron self Compton component is needed to explain GeV/TeV afterglows.^{59–61} AMEGO-X will measure afterglow spectra between hard X-ray and GeV, where the distinction between these models is most significant. Previously we have only been able to interpolate between hard X-ray and GeV energies,⁶² with the exception of a handful of NuSTAR observations.⁶³

2.3 Cosmic Ray Sources in the Galaxy

Energetic charged particles (CRs, mostly protons and electrons) are ubiquitous in our galaxy. They are accelerated in a variety of environments, such as shocks and regions with strong magnetic fields. Stellar nurseries and remnants of massive stellar explosions provide such environments. After decades of observations, two main questions regarding galactic CRs remain: in what environments are protons accelerated and what is the origin of the positron excess? AMEGO-X, with its projected sensitivity, and timing accuracy, will open the possibility to discover new galactic proton accelerators and test whether pulsars are the source of the positron excess.

2.3.1 Supernova remnants, novae, and star-formation regions

The smoking gun to identify accelerators of CR protons is to detect the characteristic neutral pion-decay ($\pi_0 \rightarrow 2\gamma$) feature, or pion bump, produced in the interaction of protons with the interstellar material. Each photon produced has an energy of 67.5 MeV (in the π_0 rest frame),⁶⁴ which is ideally matched to the AMEGO-X band. Proton acceleration is thought to happen in supernova remnants (SNRs), novae, and star-forming regions (SFRs). In SNRs, a strong shock, launched by the supernova, sweeps up the ambient medium and provides an ideal site for proton acceleration.⁶⁵ In novae, the material accreted on the white dwarf from the companion eventually undergoes explosive thermonuclear burning, creating a shock that can accelerate protons in the interaction with the companion's wind.⁶⁶ In SFRs, supernovae shocks and massive stars' winds provide the means to accelerate protons and low-energy cosmic rays (<1 TeV) play a fundamental role in shaping the chemical richness of the interstellar medium, determining the dynamical evolution of molecular clouds.^{67,68} However, even in the best-studied case (e.g., SNR IC 443; Fig. 5), the models are ambiguous, within the large observational uncertainties because of the lack of observations below 60 MeV. AMEGO-X, with its smaller PSF (factor >2) at 60 MeV than Fermi/LAT (Sec. 4), will measure the gamma-ray energy spectra of the most promising galactic hadronic accelerators, beyond SNR IC 443, including W44, and W51C; the star-forming regions Cygnus Cocoon, Westerlund 1 and 2; the recurrent T CrB and RS Oph novae and ~ 1 nova/year,⁶⁶ and will determine the gamma-ray production mechanisms to confirm potential hadronic accelerators found by Fermi/LAT. Based on extrapolating the best-fit spectra from the Fermi/LAT 4FGL DR2 catalog^{70,71} and the Fermi/LAT Supernova Remnant catalog,⁷² AMEGO-X will detect 20 to 40 other SNRs. Even if these sources show no evidence of a pion bump, studying energies below 200 MeV will allow measurements of the Bremsstrahlung emission. This, together with radio observations, will allow AMEGO-X to determine the magnetic field⁷³ in these environments and provide insight into particle acceleration in the galaxy.

2.3.2 Pulsars and pulsar wind nebulae

The flux of galactic CR positrons (electron anti-particles) in the 10 to 200 GeV range is well measured, yet it exceeds expectations from positrons generated by propagating CRs in interactions with interstellar gas.^{74,75} These additional positrons, which are referred to as a positron excess, could be produced by the known leptonic accelerators, such as pulsars, or by new physics, such as dark-matter annihilation.⁷⁶ Pulsars are the rapidly rotating remnant cores of massive stars that have collapsed and exploded leaving behind a highly magnetized neutron star. Multiwavelength observations have shown that pulsars primarily accelerate electrons and produce electron and positron pairs via interactions in their magnetospheres. These particles, accelerated by powerful magnetic fields generated by the spinning pulsar, interact with the interstellar medium and are advected into pulsar wind nebulae (PWNe).⁷⁷ There is a known population of pulsars whose peak spectral

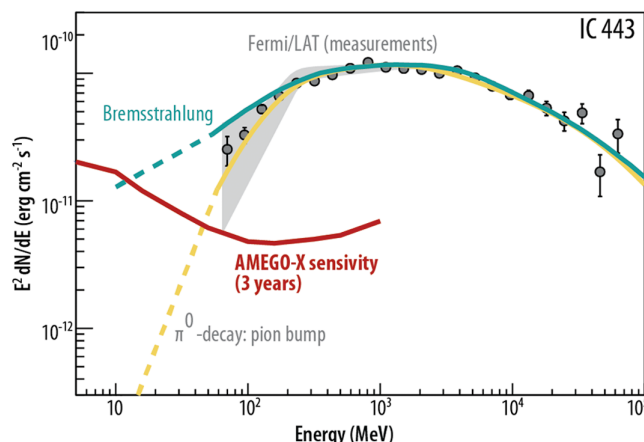


Fig. 5 Fermi/LAT SED of SNR IC 443. The green and yellow lines show the Bremsstrahlung (with break) and π^0 decay models from Ref. 69. The red solid line shows the AMEGO-X 3σ sensitivity.

energy distributions (SEDs) lie between 300 keV and 100 MeV.⁷⁸ Their signals are likely dominated by pair synchrotron radiation,⁷⁹ and they may possess very different leptonic densities relative to the population of pulsars detected by Fermi/LAT in GeV gamma rays.⁸⁰ Based on extrapolating the best-fit spectra from the Fermi/LAT catalog 4FGL DR2^{67,68} and the second Fermi/LAT catalog of gamma-ray pulsars,⁸⁰ AMEGO-X will detect more than 15 medium-energy gamma-ray peaked pulsars (mePSRs),^{78,81} observe the phase-resolved spectra of at least 5 mePSRs, and deliver 100 keV to 1 MeV polarization measurements for three pulsars (B1509-58, Vela, the Crab), testing whether synchrotron is the main emission mechanism at MeV energies. AMEGO-X will constrain the location of the emission region and the pair multiplicity (i.e., number of electrons and positrons produced), thereby, measuring the contribution of different pulsar populations to the CR positron excess.

Pulsars provide an instantaneous snapshot of the number of e^+e^- pair produced, while the surrounding PWNe provide a long-term average (tens of thousands of years) of the pairs over the life-time of the pulsar. The pulsar relativistic pairs are further accelerated at a wind termination shock at the inner nebula boundary.⁸² The energy of the pairs is regulated by synchrotron radiation losses in turbulent magnetic fields near the shock. This sets a natural scale of ~ 150 MeV for the peak of the SEDs (independent of the field strength⁸³). There PWNe acts like a calorimeter that represents the accumulation of pairs over the history of the pulsar and provides a measure of the net pair energy output. AMEGO-X will measure the e^+e^- content of more than 10 PWNe, and therefore their contribution to the CR positron excess.⁸⁴ It will also search for counterparts to the extended gamma-ray halos around middle-aged pulsars found by air shower gamma-ray experiments.^{85,86}

2.4 keV to GeV Gamma-Ray Sky

With the order of magnitude increase in sensitivity in this energy band and based on extrapolations from the Fermi/LAT 10-year source catalog⁷⁰ and Swift/BAT X-ray catalog,⁸¹ AMEGO-X will detect many additional medium-energy gamma-ray-producing sources during normal mission operations. AMEGO-X will deliver science results of significant interest to the astrophysical community and a multiyear catalog of the full medium-energy gamma-ray sky. A simulated sky map is shown in Fig. 6 covering the energy range of 1 to 30 MeV. The map includes emission from gamma-ray binaries (including accreting black holes in our galaxy), galactic diffuse continuum emission, and high-redshift blazars.^{12,89–92} The galactic diffuse emission is

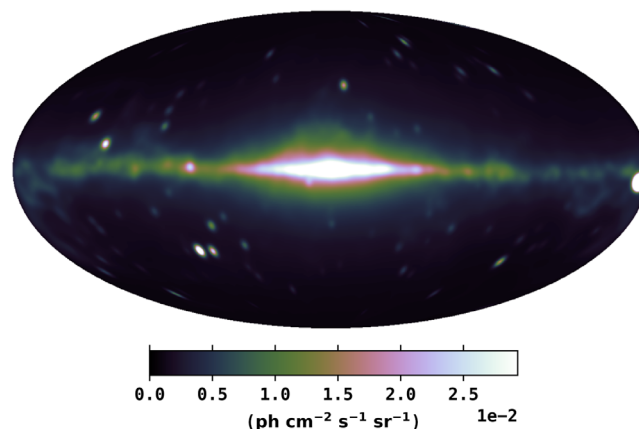


Fig. 6 Simulated AMEGO-X 3-year all-sky map in the 1-30 MeV energy range. The map contains galactic diffuse emission continuum emission calculated with GALPROP,⁸⁷ as well as individual sources extrapolated from the Fermi/LAT 4FGL-DR2 catalog⁷¹ into the AMEGO-X energy range. Blazars dominate the population (>85%) followed by pulsars. The galactic diffuse in this energy range primarily includes emission from inverse Compton and Bremsstrahlung (with contribution from π^0 at higher energy). The map is convolved with a 2D Gaussian kernel to account for the angular resolution of the instrument. We have verified that the Crab flux is in agreement with measurements.⁸⁸

calculated with GALPROP⁸⁷ and the individual sources are modeled based on an extrapolation of the Fermi/LAT 4FGL-DR2 catalog. Additional sources that will be detectable by AMEGO-X (although not shown in the sky map) include long and short GRBs, magnetar bursts and giant flares,⁹⁰ the extragalactic gamma-ray background,¹² and possibly jetted tidal disruption events^{91,93} and large-scale bubbles.⁹²

3 AMEGO-X Gamma-Ray Telescope

The gamma-ray telescope (GRT) is the AMEGO-X mission's sole instrument. It is a wide-field survey instrument designed to discover and characterize gamma-ray emission from multimessenger sources using imaging, spectroscopy, and polarization. The GRT is composed of two detector subsystems, the gamma-ray detector (GRD) and the anti-coincidence detector (ACD), which are protected by a micrometeoroid shield (MMS) (Fig. 7). The GRD consists of a tracker, with 40 layers of silicon complementary metal-oxide-semiconductor (CMOS) monolithic active pixel sensors (APS), and a calorimeter, with four layers of cesium iodide (CsI) scintillator bars. Together, they characterize gamma rays from 100 keV (25 keV for transients) to 1 GeV.⁹⁴ GRT baseline capabilities are summarized in Table 1.

The MeV range covers three different photon-matter interactions that dictate three detection techniques for GRT, as shown in Fig. 7. Between ~ 100 keV and ~ 10 MeV, photons predominantly Compton scatter. The measured position and energy of a Compton scattering interaction and subsequent absorption kinematically and geometrically constrain the initial direction of the primary gamma ray to a circle in the sky.⁹⁵ Such an event is referred to as an untracked Compton event. Compton scattering is inherently polarization sensitive, and a linearly polarized source generates a sinusoidal scattering angle distribution in the instrument.⁹⁶ If the direction of the first Compton-scattered electron is measured in the tracker, this additional kinematic information constrains the photon direction to an arc and these tracked Compton events allow for improved background rejection.⁹⁷ High-energy gamma rays (> 10 MeV) convert to an electron-positron pair, which in turn is detected through ionization tracks in the instrument. The direction of the

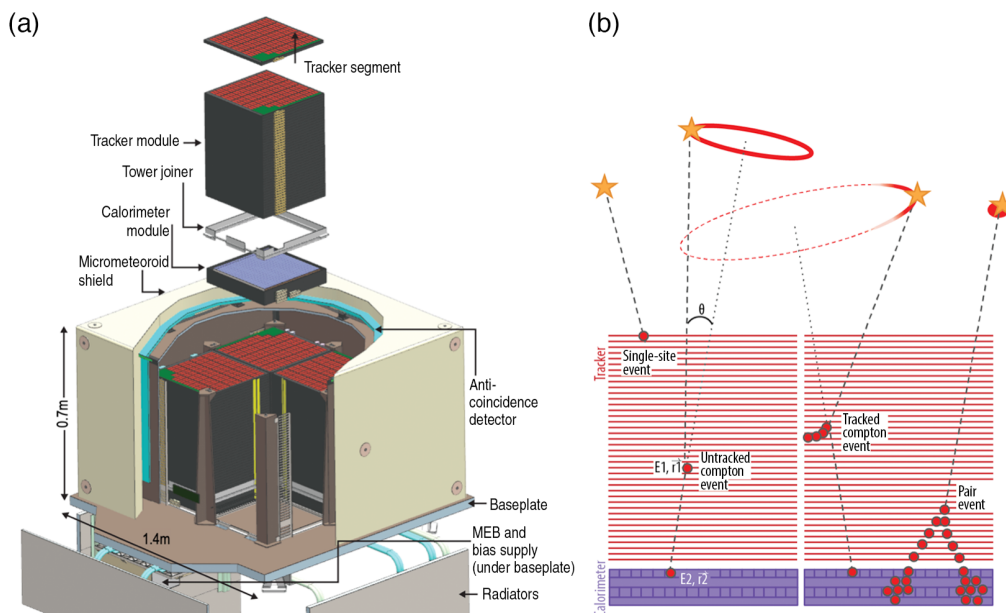


Fig. 7 (a) An exploded view of the gamma-ray telescope on board AMEGO-X. (b) The tracker (red) and calorimeter (purple) together characterize gamma-rays with three distinct detection techniques. Single-site events increase the sensitivity and low energy response (< 100 keV) for transients only. Untracked and Tracked Compton events provide imaging < 10 MeV, where the energy (E) and position (\vec{r}) of interactions are used to determine the initial Compton scatter angle (θ). Pair events enable imaging > 10 MeV using the same detection techniques as Fermi/LAT.

Table 1 Gamma-ray telescope baseline capabilities.

| Parameter | |
|-----------------------|---|
| Energy range | 25 keV to 1 GeV |
| Energy resolution | 5% FWHM at 1 MeV, 17% (68% containment half width) at 100 MeV |
| Point spread function | 4 deg FWHM at 1 MeV, 3 deg (68% containment) at 100 MeV |
| Localization accuracy | Transient: 1 deg (90% CL radius), persistent: 0.6 deg (90% CL radius) |
| Effective area | 1200 cm ² at 100 keV, 500 cm ² at 1 MeV, 400 cm ² at 100 MeV |
| Field of view | 2 π sr (<10 MeV), 2.5 sr (>10 MeV) |

incoming photon is determined from the positions of the interactions in the Tracker and the total energy is determined by the electromagnetic shower(s) detected in the calorimeter.⁹⁸

At energies below the Compton regime (<100 keV), photons predominantly undergo photo-electric absorption in a single pixel in the tracker. While these single-site events have no imaging capability, they can be used to localize transient sources using the aggregate signal.⁹⁹ For enhanced low-energy sensitivity to GRBs, AMEGO-X enables short duration (<100 s) readout of single-site events to measure emission down to the tracker threshold of 25 keV.⁹⁹

3.1 Gamma-Ray Detector

The GRD is the primary GRT science subsystem. It consists of four identical detection towers (Fig. 7), each with a tracker and calorimeter module, a dedicated low-voltage power supply (LVPS), and digital input and output (I/O) board. Although each detection tower operates independently, signals are combined in the main electronics box (MEB) such that events are reconstructed using data from the full GRD. The Towers' data acquisition (DAQ) electronics and thermal management hardware are positioned along the sides of the GRD to reduce the amount of passive material within the sensitive instrument volume.

3.1.1 Pixelated silicon tracker

The GRD tracker's main functionality is to measure the energy and position of gamma-ray and charged-particle interactions with high precision. Each of the four tracker modules consist of 40 identical stacked tracker segments (45 × 45 cm²) of silicon APS detectors, separated by 1.5 cm. The tracker segments each contain 95 Quad Chips (Fig. 8), which consist of four identical APS arrays cut out from a single silicon wafer. The AMEGO-X APS chip, AstroPix, is a 2 × 2 cm² array of 19 × 17 pixels measuring 1 × 1 mm². Each pixel contains a charge-sensitive preamplifier and comparator, where the active circuitry within the pixel results <1% loss in charge-collection volume. The APSs are 0.5 mm thick and operate at full depletion.

The major strength of the APS detectors is low noise, which is achieved through integration of the readout electronics within the detecting material. The AMEGO-X APS performance parameters have been determined through measurements of ATLASPix (designed for the ATLAS experiment at CERN)¹⁰⁰ and the first two prototype versions of AstroPix (Fig. 8), in addition to simulations from the designers at Karlsruhe Institute of Technology (KIT). AMEGO-X leverages >10 years of development in CMOS monolithic active pixel silicon detectors from ground-based particle physics experiments.^{101–104} By optimizing these APSs for space applications^{100,105} the detectors enable observations at lower photon energies, achieve an overall increase in sensitivity, and are simpler to integrate compared with previous silicon detector technologies.

The GRT design uses minimal passive material and carbon fiber-reinforced polymers to reduce photon attenuation and backgrounds from activation. In this regard, the tracker is designed with high thermal conductivity K1100/Cyanate Ester (CE) for heat extraction from

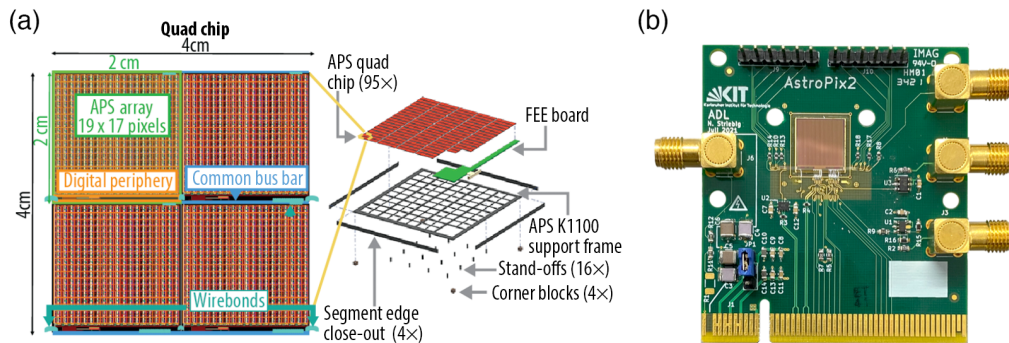


Fig. 8 (a) The AMEGO-X Tracker relies on low-noise, low power CMOS monolithic APS detectors. Each Quad Chip consists of four identical APS arrays of 19×17 pixels, with the digital periphery located at the bottom of each APS array. Each Tracker Segment consists of 95 Quad Chips with a common bus bar for power distribution and wirebonds utilizing SPI readout. The Quad Chips are supported with a K1100 carbon fiber frame. (b) The prototype AstroPix_v2 detector, a 1×1 cm chip, has been fabricated and tested on the bench and in heavy ion beam tests.

the APS detectors. The APS support frame (Fig. 8) is CNC cut K1100/CE laminate bonded to M55J/CE perimeter closeouts and stand-offs for additional stiffness.

3.1.2 Hodoscopic CsI calorimeter

The main functionality of the calorimeter is to measure the position and energy of Compton-scattered photons and the electromagnetic showers produced from electron and positron pairs over a broad energy range. Situated directly below the tracker subsystem, the Calorimeter is composed of four layers of thallium-doped cesium iodide (CsI:TI) bars, hodoscopically arranged. One of the four calorimeter modules is shown in Fig. 9.

Each layer consists of 25 bars, each with a dimension of $1.5 \times 1.5 \times 38$ cm³. The bars are wrapped in reflective material to pipe scintillation photons to each end, where readout occurs via an array of silicon photomultipliers (SiPMs). To achieve a large dynamic range in a single Calorimeter bar and to mitigate the effects of saturation, a mixture of small and large ONSem SiPMs are used to cover two gain ranges,¹⁰⁶ as shown in Fig. 9. Each end of each CsI bar is read out with a low energy SiPM array, which is a sum of eight 3×3 mm² SiPMs, and a high energy array, which is a sum of four 1×1 mm² SiPMs. Although SiPMs are sensitive to damage from the orbital radiation environment, work done at NRL has demonstrated that the damage effects can be successfully mitigated by proper instrument configuration without affecting instrument performance.^{107–109} The position of the interaction along the bar is determined from the relative amplitude of signals on each end.

The AMEGO-X Calorimeter utilizes a design based on Fermi/LAT.⁹⁸ The Calorimeter team at Naval Research Laboratory (NRL) designed, developed, assembled, tested, and currently

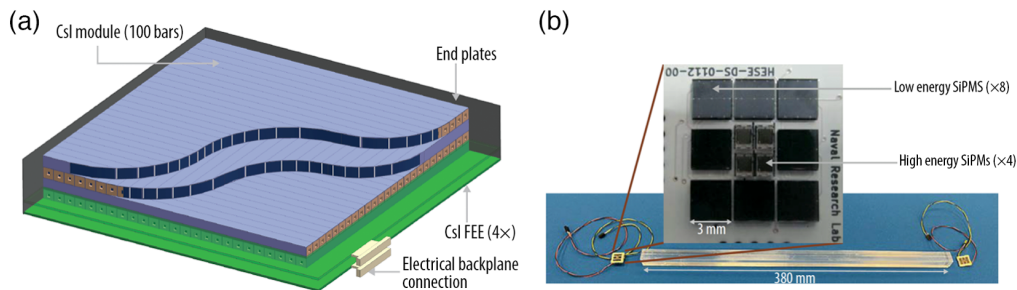


Fig. 9 (a) The GRT hodoscopic arrangement of four Calorimeter layers enables an accurate measurement of gamma-ray energies through the profile of electromagnetic showers. (b) The dual-gain SiPM readout at the ends of each CsI bar has been demonstrated in the lab and enables low-noise readout across a large dynamic range.

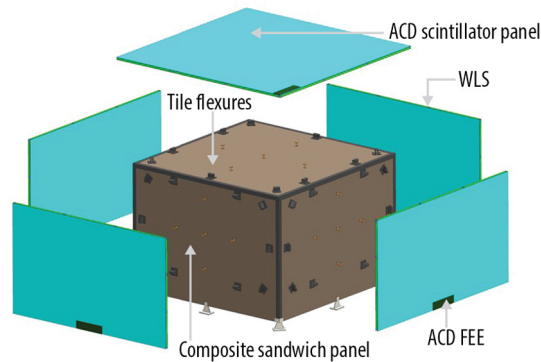


Fig. 10 The AMEGO-X ACD is a simple, nonsegmented version of the Fermi/LAT design. The ACD consists of five scintillation panels read out through wave-length shifting (WLS) bars with SiPM arrays on each end. The ACD surrounds the GRD to veto incident charged particles, reducing the background rate during flight.

operates the Fermi/LAT CsI Calorimeter. Furthermore, the team has built and demonstrated the performance of a prototype AMEGO-X GRT Calorimeter with SiPM readout in gamma-ray beam tests.^{106,110}

3.2 Anti-Coincidence Detector

AMEGO-X uses a dedicated anti-coincidence detector (ACD) to reduce the significant cosmic-ray background. The ACD comprises five plastic scintillator panels that surround the GRD to enable vetos associated with incident charged particles while being transparent to gamma rays (Fig. 10). Each ACD panel has three wavelength-shifting bars (WLS) on each of its four edges. Scintillation light entering the WLS bars is transmitted to the ends, where signals are measured by arrays of $6 \times 6 \text{ mm}^2$ ONSemi SiPMs. Each WLS is read out independently to recover the energy deposited in each ACD panel. The ACD has an energy threshold of 200 keV, which is well below the minimum ionizing particle (MIP) average energy deposition of 2.5 MeV. The ACD interfaces directly with the MEB, which provides I/O and FEE power.

4 Instrument Performance

For Compton and pair telescopes, much of the performance relies on accurate event reconstruction and background rates, and therefore simulations were performed with the state-of-the-art MEGAlib analysis package,¹¹¹ which is built around Geant4.¹¹² A detailed mass model that reproduces the active and passive material is simulated with the detector performance to determine interactions of photons and particles and the resulting measured signals.

4.1 Background Model

Background radiation is one of the dominant factors that can limit the sensitivity of an MeV telescope, and therefore detailed background simulations are necessary for accurate performance predictions. The background models used in MEGAlib are based on measurements by COMPTEL,¹¹³ INTEGRAL/SPI,¹¹⁴ Fermi/LAT,¹¹⁵ and NuSTAR,¹¹⁶ and cosmic-ray population measurements, with an assumed AMEGO-X orbit of 575 km and an inclination of 6 deg. The models and components (including prompt and delayed emission from cosmic-rays, extragalactic diffuse, and Albedo emission) are orbit averaged and are described in more detail in Ref. 117.

The measured signals from charged cosmic rays are the significant background to gamma-ray observations, but almost all of these events can be vetoed by the ACD. Another background-rejection capability is through event reconstruction; only events that have a valid Compton sequence or pair-conversion tracks will be identified as “good” events for higher-level analysis. Figure 11 shows the resulting measured background spectrum after the ACD veto and event

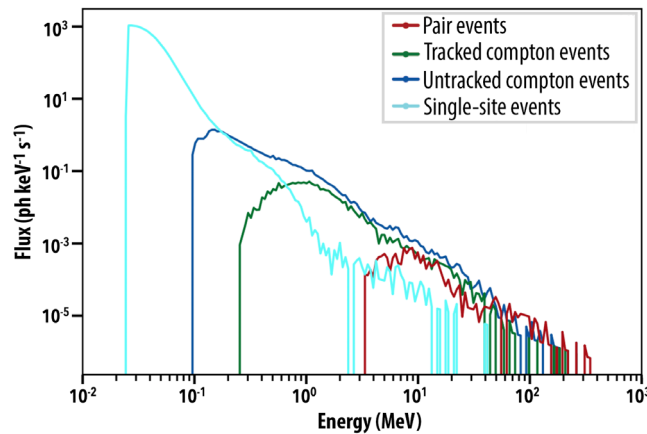


Fig. 11 The expected measured rates for each event type from the MEGAlib background models. The event classification is performed in MEGAlib, and the dominant background at lower energies is cosmic and atmospheric photons, while at higher energies in the Compton regime, the delayed emission of activated material in the instrument is the dominant source of background. The majority of background events >1 MeV are classified as untracked Compton events because this is the most nonrestrictive event class.

reconstruction, separated for each event type as classified by MEGAlib.⁹⁹ The most significant background rate is measured at low energies as single-site events, which correspond to a single triggered pixel in the tracker. This measured flux is dominated by cosmic and atmospheric photons, and without imaging capabilities to separate any source emission from background, single-site events can only be used for transient detection when the source rate is high. Most background events that have more than one trigger in the GRT, but are not vetoed by the ACD and do not leave clear straight charged-particle tracks in the tracker, are classified as Untracked Compton events, since that is the most inclusive event category in MEGAlib. The dominant background component in the Compton regime is activation of the passive and active instrument material by cosmic rays, where the delayed emission of radiation cannot be vetoed by the ACD. In the pair regime, the dominant background is albedo photons,¹¹⁷ which also are not vetoed by the ACD.

Further background rejection can be achieved through fine-tuned event selections depending on the observation, such as the total photon energy, pair opening angle, Compton scatter angle, or distance between interactions.

4.2 Angular Resolution and Effective Area

Monoenergetic point source simulations are performed in MEGAlib to determine the energy resolution, effective area, and angular resolution of AMEGO-X. Figure 12 shows the measured angular resolution and effective area as a function of energy for each event classification from these simulations. The angular resolution in the Compton regime is defined as the FWHM of the angular resolution measure (ARM) histogram, which is a projection of the point spread function in one dimension, as is standard for Compton telescopes. In the pair regime, the angular resolution is defined as the 68% containment radius, following the standard Fermi/LAT definition. There is no angular resolution for the single-site events since there are no imaging capabilities from these interactions.

The predicted angular resolution is 4 deg at 1 MeV and 2.5 deg at 100 MeV. Measuring the track of a Compton-scattered electron does not improve the angular resolution in the Compton regime as the uncertainty in the scattering angle is often large. The angular resolution for tracked Compton events is in fact slightly worse than those for untracked Compton events due to the inherent selection of events that have larger scattering angles. Also shown in Fig. 12 are the measured angular resolution of COMPTEL, Fermi/LAT, and the requirements for COSI. The angular resolution of AMEGO-X is better than Fermi/LAT since the LAT's resolution is limited by multiple scattering in the tungsten conversion foils within the tracker.

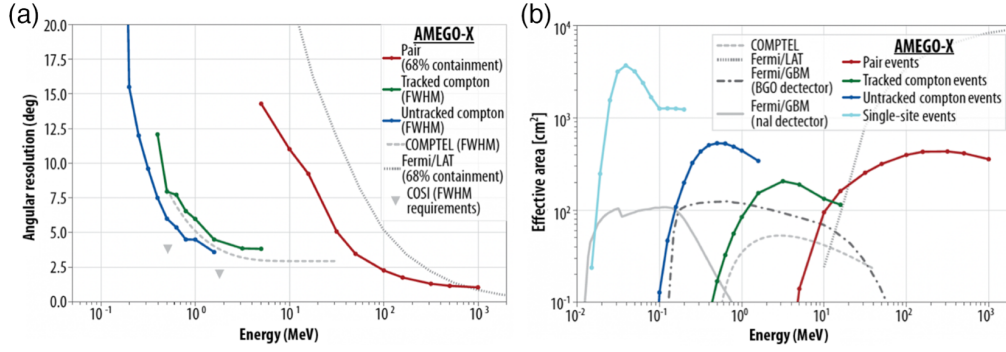


Fig. 12 (a) The projected angular resolution and (b) effective area are determined through on-axis, mono-energetic, point source simulations. In addition to background rate, these parameters are the main contribution to the sensitivity of the instrument.

The simulated effective area, shown in Fig. 12, is a measure of the detection efficiency of the telescope. It is defined as the required area of an ideal detector, i.e. 100% efficient, to detect an equivalent number of photons. It is calculated here as the number of valid events classified by MEGALib divided by the initial number of simulated photons, and scaled by the area of the mass model's surrounding sphere. The expected effective area is 1200 cm² at 100 keV, 500 cm² at 1 MeV, and 400 cm² at 100 MeV. Figure 12 also shows the effective area for a single Fermi/GBM BGO and NaI detector, as well as COMPTEL and Fermi/LAT.

4.2.1 Continuum and transient sensitivity

The sensitivity of AMEGO-X is determined for steady-state (i.e., continuum) sources and transient sources based on the above MEGALib simulated performance parameters. From the measured effective area, angular resolution, and energy resolution, the continuum sensitivity can be calculated as the minimum detectable source flux

$$F_{\min}(E) = \frac{n^2 + n\sqrt{n^2 + 4N_b}}{2A_{\text{eff}}T_{\text{Obs}}},$$

where n is the required detection significance (3σ) per energy band, N_b is the number of background counts, A_{eff} is the effective area, and T_{Obs} is the observation time. The 3-year AMEGO-X sensitivity is shown in Fig. 13. To account for the survey-mode observation, the effective area is conservatively taken from simulations of sources at 37 deg off-axis, and the observation time is estimated to be 20% of the full mission ($T_{\text{Obs}} = 3 \text{ yr} \times 0.2$).

The continuum sensitivity is calculated for untracked Compton, tracked Compton, and pair events separately. When there are significant contributions from two event types, e.g., pair events at 10 MeV have a similar effective area to tracked events at this energy, the sensitivities are combined

$$F_{\text{combined}} = F_{\text{tracked}} \sqrt{\frac{F_{\text{pair}}}{F_{\text{tracked}} + F_{\text{pair}}}}.$$

The continuum sensitivity is $3.2 \times 10^{-12} \text{ erg/cm}^2/\text{s}$ at both 1 and 100 MeV. The regime where Compton and pair events overlap, around 10 MeV, has worse sensitivity due to the limited classification capability currently implemented in MEGALib. Recent developments in event identification and reconstruction with neural networks have shown dramatic improvements in sensitivity.¹¹⁸ Additionally, the projected performance in the pair regime ($>10 \text{ MeV}$) is expected to improve, as MEGALib does not currently include reconstruction and shower profiling techniques developed for Fermi/LAT.¹¹⁹

The transient sensitivity is determined from the measured signal-to-noise ratio from simulations of canonical GRBs. It is defined for each event type (single site and Compton)

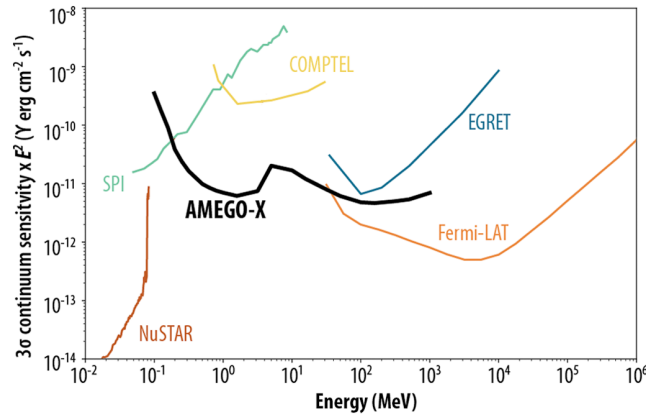


Fig. 13 The AMEGO-X continuum sensitivity using untracked Compton, tracked Compton, and pair events is shown for the 3 year mission compared with the sensitivity of past and present missions. The effective area is conservatively taken to be for sources 37 deg off-axis, and the observation time is estimated to be 20% of the full mission ($T_{\text{Obs}} = 3 \text{ yr} \times 0.2$).

$$\text{SN} = \frac{S}{\sqrt{S + B}},$$

where S is the number of source counts detected (from GRB source simulations) and B is the number of background counts (from background simulations). The minimum detectable flux at which the combined SN ratios $F_{\text{min}} = \sqrt{\text{SN}_{\text{single site}}^2 + \text{SN}_{\text{Compton}}^2} \geq 6.5\sigma$ and $\text{SN}_{\text{Compton}} \geq 4.5\sigma$ is the transient sensitivity. The AMEGO-X transient sensitivity is $0.5 \gamma/\text{cm}^2/\text{s}$ between 25 keV and 1 MeV for 1 s. The derived GRB rates account for the dependence of the effective area with off-axis angle, and the transient sensitivity is described in Ref. 99.

5 AMEGO-X Mission Implementation

5.1 Spacecraft

The AMEGO-X flight system consists of the GRT instrument integrated onto a spacecraft bus which leverages Lockheed Martin Space's (LMS) standard subsystem architectures (Fig. 14). These include structure, mechanisms, power, attitude determination and control (ADCS), C&DH, and flight software (FSW) from cost-capped planetary missions dating back >15 years,

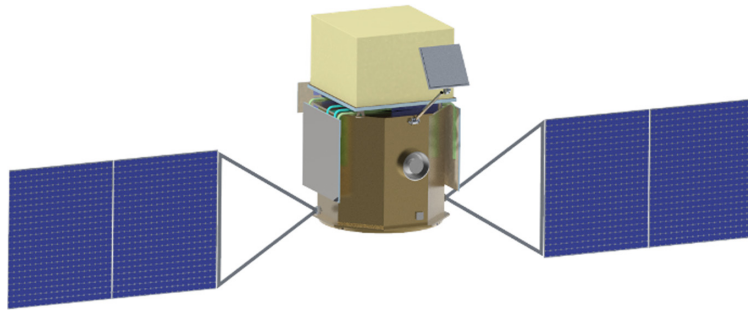


Fig. 14 The gamma-ray telescope (yellow box) is shown on top of a base plate attached to the spacecraft bus. The pair of single-axis gimbaled solar arrays from end to end are approximately 11 m wide. This figure illustrates the deployed high-gain antenna, and one of the two low-gain antennae attached to the spacecraft bus. The other low-gain antenna is on the back side. Radiators (also gray) are located on each side of the spacecraft bus other than the side with the high-gain antenna.

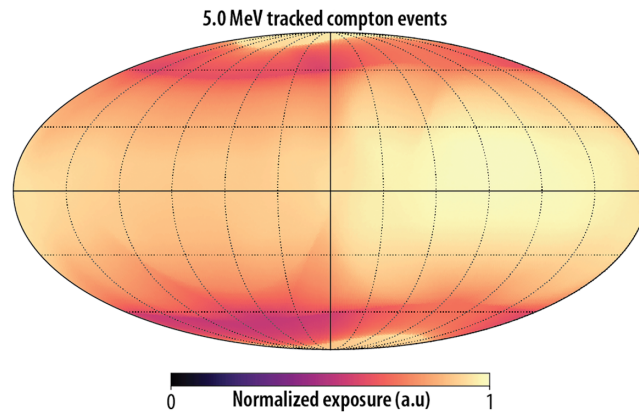


Fig. 15 The normalized exposure map for 5 MeV gamma rays (as an illustration) assuming low-Earth orbit (600 km) with a low inclination (5 deg). Rocking alternately $\pm 30^\circ$ deg from zenith every orbit enables the GRT to uniformly observe nearly the entire sky every two orbits (~ 3 h). Over the course of 24 h, the GRT survey covers the entire sky.

and hardware and software from LMS spacecraft including MAVEN, Lucy, IRIS, OSIRIS-REx, and Juno.

5.2 Observation Plan

AMEGO-X has been proposed to launch into Low Earth Orbit (LEO) in 2028 to start a 3-year baseline science campaign with the potential for an extended mission. Science campaign operations are straight-forward, consisting of scanning the sky with the GRT instrument 30° deg north or south of zenith every other orbit, providing a nearly all-sky view every two orbits (Fig. 15). The baseline AMEGO-X LEO orbit (Fig. 15) is circular with a 600 km altitude and inclination of 5° . This inclination provides the low background radiation environment needed to achieve the required GRT sensitivity.

5.2.1 Science data plan and products

The AMEGO-X mission performs observations of the full medium energy gamma-ray sky every 3 h. The data include four different gamma-ray event classes distinguished by the energy of the incoming gamma-ray: single-site (photoelectric absorption, used only for fast transients), Compton (tracked or untracked), and pair events.

AMEGO-X data will be event-based, where each gamma-ray interaction in the instrument is analyzed separately. Images, light curves, polarization analysis, and other science products are generated on the ground as illustrated in Fig. 16. For the rapid detection and localization of gamma-ray transients, AMEGO-X uses on-board transient alert (TA) logic based on Fermi/GBM algorithms.^{120,121} TAs are identified by the MEB CPU as a significant (6.5σ) rate increase above the background through a combination of Tracker triggers and events with triggers in tracker and calorimeter. Based on simulations, TAs are expected 3 to 5/day and the probability of a false TA detection is <1 per year.

The AMEGO-X data plan identifies multiple levels of scientific data products that begin as raw binary files downlinked from the spacecraft and end as scientific data products, such as source spectra and light curves. Users download photon and housekeeping data from the science archive, along with instrument response functions, diffuse maps, and source lists used to perform analyses on any time, energy, and area scale. The TA data contains the spacecraft attitude information, a coarsely binned light curve, and localization from on-board event reconstruction. After straightforward science operations center (SOC) processing, the TA is sent to the Gamma-ray coordinates network (GCN) to enable multiwavelength follow-up. After the survey data is processed on the ground, a more accurate localization and full light curves will update the initial GCN alert. The GRT instrument team will provide python-based analysis tools and tutorials

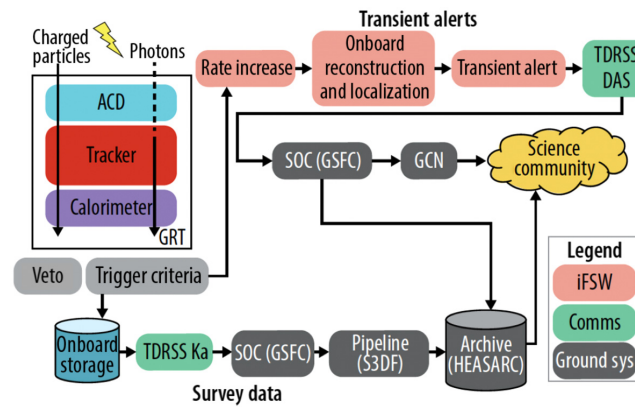


Fig. 16 The two main science data products, transient alerts and survey data, use the same mode of operation and pipeline, but different telemetry paths. Transient alerts (90% in 30 s) use tracking and data relay satellite system (TDRSS) for rapid alerts to the gamma-ray coordinates network (GCN) for multimessenger and multiwavelength follow-up. All-sky survey data (90% in 24 h) is telemetered via TDRSS Ka band two to three times per day for on-ground processing and dissemination to the science community.

to make AMEGO-X data accessible to the scientific community, similar to Fermi/LAT¹²² and current tools being developed for COSI. Photon and spacecraft data will be accessible through a custom photon data server (similar to Fermi/LAT). Weekly photon and spacecraft files, all catalogs, and higher-level data products will be available via the high-energy astrophysics science archive research center (HEASARC).

6 Summary

AMEGO-X will deliver breakthrough discoveries as a MIDEX class mission addressing areas highlighted as the highest scientific priority for explorer-scale missions in the Astro2020 Decadal Survey Report: multimessenger astrophysics and time-domain astronomy. During its 3 year mission, it will survey the gamma-ray sky with unprecedented sensitivity in the energy range from 100 keV to 1 GeV. The gamma-ray telescope design is well understood with a combination of instrument subsystems that leverage large investments in detector technologies by the Department of Energy, now tailored for space use, while also taking advantage of the extensive flight heritage from Fermi. Its all-sky coverage enables a sensitivity to transients from milliseconds to years. AMEGO-X is complementary to Fermi and COSI with broad MeV continuum, transient, and polarization capabilities.

The AMEGO-X team has experts from Fermi and COSI who have built the instruments, simulation software, data pipelines, and data analysis tools. AMEGO-X's spacecraft partner, Lockheed Martin space (LMS), has a demonstrated track record of successful Explorer-class bus design and operation. The AMEGO-X science and instrument teams include members from NASA GSFC, Argonne National Laboratory, the Naval Research Laboratory, and LMS, as well as university science partners who are members of the LIGO Collaboration, the IceCube Collaboration, and the Cherenkov Telescope Array Consortium. Together, the science team will ensure the maximum return from this unique and groundbreaking mission.

Acknowledgments

The authors would like to acknowledge generous ongoing support from a number of agencies and institutes that have supported the development of the AMEGO-X mission concept. These include NASA Goddard Space Flight Center, the Naval Research Laboratory, and Argonne National Laboratory. The material is based upon work supported by NASA under award number 80GSFC21M0002. We also acknowledge the contributions to the design of the AMEGO-X spacecraft by Jonathan Hartley and Lindsay Papsidero from Lockheed Martin Space and

the design of the AMEGO-X instrument by the engineering team at Goddard Space Flight Center.

References

1. Committee for a Decadal Survey on Astronomy and Astrophysics, “Pathways to discovery in astronomy and astrophysics for the 2020s,” <https://www.nationalacademies.org/our-work/decadal-survey-on-astronomy-and-astrophysics-2020-astro2020> (2021).
2. “2021 astrophysics medium explorers (MIDEX),” <https://explorers.larc.nasa.gov/2021APMIDEX/MIDEX/index.html> (2020).
3. J. A. Tomsick, “The Compton spectrometer and imager project for MeV astronomy,” in *PoS ICRC2021*, p. 652 (2021).
4. K. S. Hirata et al., “Observation in the Kamiokande-II detector of the neutrino burst from supernova sn1987a,” *Phys. Rev. D* **38**, 448–458 (1988).
5. IceCube Collaboration, “Neutrino emission from the direction of the blazar TXS 0506+056 prior to the icecube-170922a alert,” *Science* **361**(6398), 147–151 (2018).
6. IceCube, Fermi/LAT, MAGIC et al., “Multimessenger observations of a flaring blazar coincident with high-energy neutrino icecube-170922a,” *Science* **361**(6398), eaat1378 (2018).
7. B. P. Abbott et al., “GW170817: observation of gravitational waves from a binary neutron star inspiral,” *Phys. Rev. Lett.* **119**(16), 161101 (2017).
8. B. P. Abbott et al., “Multi-messenger observations of a binary neutron star merger,” *Astrophys. J. Lett.* **848**(2), L12 (2017).
9. C. M. Urry and P. Padovani, “Unified schemes for radio-loud active galactic nuclei,” *Publ. Astron. Soc. Pac.* **107**, 803 (1995).
10. M. Boettcher et al., “Leptonic and hadronic modeling of fermi-detected blazars,” *Astrophys. J.* **768**, 54 (2013).
11. H. Zhang and M. Böttcher, “X-ray and gamma-ray polarization in leptonic and hadronic jet models of blazars,” *Astrophys. J.* **774**, 18 (2013).
12. M. Ajello et al., “The evolution of Swift/BAT blazars and the origin of the MeV background,” *ApJ* **699**, 603–625 (2009).
13. Y. Inoue et al., “Prospect for future MeV gamma-ray active galactic nuclei population studies,” *Publ. Astron. Soc. Jpn.* **67**, 76 (2015).
14. N. Tsuji et al., “Cross-match between the latest Swift-BAT and Fermi-LAT Catalogs,” *Astrophys. J.* **916**(1), 28 (2021).
15. S. Abdollahi et al., “The second catalog of flaring gamma-ray sources from the fermi all-sky variability analysis,” *Astrophys. J.* **846**, 34 (2017).
16. A. Mücke and R. J. Protheroe, “A Proton synchrotron blazar model for flaring in Markarian 501,” *Astropart. Phys.* **15**, 121–136 (2001).
17. K. Mannheim, “The Proton blazar,” *Astron. Astrophys.* **269**, 67 (1993).
18. A. Keivani et al., “A Multimessenger picture of the flaring blazar TXS 0506+056: implications for high-energy neutrino emission and cosmic ray acceleration,” *Astrophys. J.* **864**(1), 84 (2018).
19. A. Reimer, M. Böttcher, and S. Buson, “Erratum: cascading constraints from neutrino-emitting blazars: the case of TXS 0506+056 (2019, ApJ, 881, 46),” *Astrophys. J.* **899**, 168 (2020).
20. R. Xue et al., “A two-zone blazar radiation model for “Orphan” neutrino flares,” *Astrophys. J.* **906**, 51 (2021).
21. T. R. Lewis et al., “Modeling and simulations of TXS 0506+056 Neutrino events in the MeV band,” arXiv 2111.10600 (2021).
22. K. Murase, D. Guetta, and M. Ahlers, “Hidden cosmic-ray accelerators as an origin of TeV-PeV cosmic neutrinos,” *Phys. Rev. Lett.* **116**(7), 071101 (2016).
23. M. G. Aartsen et al., “The IceCube realtime alert system,” *Astropart. Phys.* **92**, 30–41 (2017).
24. F. Krauß et al., “Fermi/LAT counterparts of IceCube neutrinos above 100 TeV,” *Astron. Astrophys.* **620**, A174 (2018).

25. M. G. Aartsen et al., “Time-integrated neutrino source searches with 10 years of IceCube data,” *Phys. Rev. Lett.* **124**(5), 051103 (2020).
26. M. Cerruti et al., “Gammas and neutrinos from TXS 0506+056,” in *Week of French Astrophys.: Semaine de l’Astrophysique Francaise* (2018).
27. K. Murase, F. Oikonomou, and M. Petropoulou, “Blazar flares as an origin of high-energy cosmic neutrinos?” *Astrophys. J.* **865**(2), 124 (2018).
28. V. S. Paliya et al., “Leptonic and hadronic modeling of *Fermi*-LAT hard spectrum quasars and predictions for high-energy polarization,” *Astrophys. J.* **863**(1), 98 (2018).
29. H. Zhang et al., “Probing the emission mechanism and magnetic field of neutrino blazars with multiwavelength polarization signatures,” *Astrophys. J.* **876**(2), 109 (2019).
30. M. C. Weisskopf et al., “The imaging X-ray polarimetry explorer (IXPE): pre-launch,” *J. Astron. Telesc. Instrum. Syst.* **8**, 026002 (2022).
31. A. L. Peirson, I. Liodakis, and R. W. Romani, “Testing high-energy emission models for blazars with x-ray polarimetry,” *Astrophys. J.* **931**(1), 59 (2022).
32. M. G. Aartsen et al., “Characteristics of the diffuse astrophysical electron and tau neutrino flux with six years of IceCube high energy cascade data,” *Phys. Rev. Lett.* **125**(12), 121104 (2020).
33. A. Merloni and A. C. Fabian, “Accretion disc coronae as magnetic reservoirs,” *Mon. Not. R. Astron. Soc.* **321**, 549–552 (2001).
34. Y. Inoue and A. Doi, “Detection of coronal magnetic activity in nearby active supermassive black holes,” *Astrophys. J.* **869**, 114 (2018).
35. Y. Inoue et al., “On high-energy particles in accretion disk coronae of supermassive black holes: implications for MeV gamma rays and high-energy neutrinos from AGN cores,” RIKEN-iTHEMS-Report 19 (2019).
36. K. Murase, S. S. Kimura, and P. Meszaros, “hidden cores of active galactic nuclei as the origin of medium-energy neutrinos: critical tests with the MeV gamma-ray connection,” *Phys. Rev. Lett.* **125**(1), 011101 (2020).
37. B. P. Abbott et al., “Prospects for observing and localizing gravitational-wave transients with Advanced LIGO, Advanced Virgo and KAGRA,” *Living Rev. Relativ.* **23**, 3 (2020).
38. B. P. Abbott et al., “Gravitational waves and gamma-rays from a binary neutron star merger: GW170817 and GRB 170817a,” *Astrophys. J.* **848**, L13 (2017).
39. B. D. Metzger, “Welcome to the multi-messenger era! Lessons from a neutron star merger and the landscape ahead,” arXiv 1710.05931 (2017).
40. B. P. Abbott et al., “GW190425: observation of a compact binary coalescence with total mass: 3.4 Me,” *Astrophys. J. Lett.* **892**, L3 (2020).
41. T. Sakamoto et al., “LIGO/Virgo S190425z: Swift/BAT counterpart search,” in *GRB Coord. Network 24184*, p. 1 (2019).
42. C. FletcherFermi-GBM Team, and GBM-LIGO/Virgo Group, “LIGO/Virgo S190425z: fermi GBM observations,” in *GRB Coord. Network 24185*, p. 1 (2019).
43. E. Burns, “Neutron star mergers and how to study them,” *Living Rev. Relativ.* **23**(1), 4 (2020).
44. B. Margalit and B. D. Metzger, “The Multi-messenger matrix: the future of neutron star merger constraints on the nuclear equation of state,” *Astrophys. J. Lett.* **880**(1), L15 (2019).
45. V. Connaughton et al., “Localization of gamma-ray bursts using the fermi gamma-ray burst monitor,” *Astrophys. J. Suppl. Ser.* **216**(2), 32 (2015).
46. A. Goldstein et al., “Evaluation of automated fermi GBM localizations of gamma-ray bursts,” *Astrophys. J.* **895**(1), 40 (2020).
47. E. J. Howell et al., “Joint gravitational wave - gamma-ray burst detection rates in the aftermath of GW170817,” *Mon. Not. R. Astron. Soc.* **485**, 1435–1447 (2019).
48. L. Resmi et al., “Low-frequency view of GW170817/GRB 170817A with the giant metrewave radio telescope,” *Astrophys. J.* **867**, 57 (2018).
49. R. Margutti et al., “The binary neutron star event LIGO/Virgo GW170817 160 days after merger: synchrotron emission across the electromagnetic spectrum,” *Astrophys. J. Lett.* **856**, L18 (2018).
50. D. Steeghs et al., “The gravitational-wave optical transient observer (GOTO): prototype performance and prospects for transient science,” *Mon. Not. R. Astron. Soc.* **511**(2), 2405–2422 (2022).

51. E. C. Bellm et al., “The Zwicky transient facility: system overview, performance, and first results,” *Publ. Astron. Soc. Pac.* **131**, 018002 (2019).
52. Ž. Ivezić et al., “LSST: from science drivers to reference design and anticipated data products,” *Astrophys. J.* **873**, 111 (2019).
53. K. P. Mooley et al., “Superluminal motion of a relativistic jet in the neutron-star merger GW170817,” *Nature* **561**, 355–359 (2018).
54. D. Lazzati et al., “Off-axis emission of short γ -ray bursts and the detectability of electromagnetic counterparts of gravitational-wave-detected binary mergers,” *Mon. Not. R. Astron. Soc.* **471**, 1652–1661 (2017).
55. X. Xie, J. Zrake, and A. MacFadyen, “Numerical simulations of the jet dynamics and synchrotron radiation of binary neutron star merger event GW170817/GRB 170817A,” *Astrophys. J.* **863**(1), 58 (2018).
56. R. Abbott et al., “Population properties of compact objects from the second LIGO-virgo gravitational-wave transient catalog,” *Astrophys. J. Lett.* **913**(1), L7 (2021).
57. M. M. Kasliwal et al., “Illuminating gravitational waves: a concordant picture of photons from a neutron star merger,” *Science* **358**, 1559–1565 (2017).
58. F. Foucart, “A brief overview of black hole-neutron star mergers,” *Front. Astron. Space Sci.* **7**, 46 (2020).
59. M. Ackermann et al., “Fermi-LAT observations of the gamma-ray burst GRB 130427A,” *Science* **343**, 42–47 (2014).
60. H. Abdalla et al., “A very-high-energy component deep in the γ -ray burst afterglow,” *Nature* **575**, 464–467 (2019).
61. MAGIC Collaboration et al., “Observation of inverse Compton emission from a long γ -ray burst,” *Nature* **575**, 459–463 (2019).
62. M. Ajello et al., “Investigating the nature of late-time high-energy GRB emission through joint fermi/swift observations,” *Astrophys. J.* **863**, 138 (2018).
63. C. Kouveliotou et al., “NuSTAR observations of GRB 130427A establish a single component synchrotron afterglow origin for the late optical to multi-GeV emission,” *Astrophys. J. Lett.* **779**, L1 (2013).
64. F. W. Stecker, *Cosmic Gamma Rays*, Vol. 249, Mono Book Corp., Baltimore (1971).
65. D. Caprioli, “Understanding hadronic gamma-ray emission from supernova remnants,” *J. Cosmol. Aatropart. Phys.* **05**, 026 (2011).
66. L. Chomiuk, B. D. Metzger, and K. J. Shen, “New insights into classical novae,” *Ann. Rev. Astron. Astrophys.* **59**, 391–444 (2021).
67. M. Ackermann et al., “A cocoon of freshly accelerated cosmic rays detected by fermi in the cygnus superbubble,” *Science* **334**, 1103 (2011).
68. M. Padovani et al., “Impact of low-energy cosmic rays on star formation,” *Space Sci. Rev.* **216**, 29 (2020).
69. M. Ackermann et al., “Detection of the characteristic pion-decay signature in supernova remnants,” *Science* **339**, 807–811 (2013).
70. S. Abdollahi et al., “Fermi large area telescope fourth source catalog,” *Astrophys. J. Suppl.* **247**(1), 33 (2020).
71. J. Ballet et al., “Fermi large area telescope fourth source catalog data release 2,” *Astrophys. J. Suppl.* **247**, 33 (2020).
72. F. Acero et al., “The first fermi LAT supernova remnant catalog,” *Astrophys. J. Suppl.* **224**(1), 8 (2016).
73. R. Cowsik and S. Sarkar, “A lower limit to the magnetic field in Cassiopeia-A,” *Mon. Not. R. Astron. Soc.* **191**, 855–861 (1980).
74. M. Ackermann et al., “Measurement of separate cosmic-ray electron and positron spectra with the fermi large area telescope,” *Phys. Rev. Lett.* **108**, 011103 (2012).
75. M. Aguilar et al., “First result from the alpha magnetic spectrometer on the international space station: precision measurement of the positron fraction in primary cosmic rays of 0.5–350 GeV,” *Phys. Rev. Lett.* **110**, 141102 (2013).
76. I. Cholis and D. Hooper, “Dark matter and pulsar origins of the rising cosmic ray positron fraction in light of new data from AMS,” *Phys. Rev. D* **88**, 023013 (2013).

77. P. Slane, “Pulsar wind nebulae,” in *Handbook of Supernovae*, A. Alsabti and P. Murdin, Eds., Springer, Cham (2017).
78. L. Kuiper and W. Hermsen, “The soft γ -ray pulsar population: a high-energy overview,” *Mon. Not. R. Astron. Soc.* **449**, 3827–3866 (2015).
79. A. K. Harding and C. Kalapotharakos, “Multiwavelength polarization of rotation-powered pulsars,” *Astrophys. J.* **840**(2), 73 (2017).
80. A. A. Abdo et al., “The second fermi large area telescope catalog of gamma-ray pulsars,” *Astrophys. J. Suppl.* **208**, 17 (2013).
81. K. Oh et al., “The 105 month Swift-BAT all-sky hard X-ray survey,” *Astrophys. J. Suppl.* **235**(1), 4 (2018).
82. C. F. Kennel and F. V. Coroniti, “Magnetohydrodynamic model of crab nebula radiation,” *Astrophys. J.* **283**, 710–730 (1984).
83. O. C. de Jager et al., “Gamma-ray observations of the crab nebula: a study of the synchro-compton spectrum,” *Astrophys. J.* **457**, 253 (1996).
84. M. Di Mauro, S. Manconi, and F. Donato, “Prospects for the detection of synchrotron halos around middle-age pulsars,” *Bull. Am. Astron. Soc.* **51**, 183 (2019).
85. A. U. Abeysekara et al., “Extended gamma-ray sources around pulsars constrain the origin of the positron flux at Earth,” *Science* **358**(6365), 911–914 (2017).
86. F. Aharonian et al., “Extended very-high-energy gamma-ray emission surrounding PSR J0622+3749 Observed by LHAASO-KM2A,” *Phys. Rev. Lett.* **126**(24), 241103 (2021).
87. I. V. Moskalenko and A. W. Strong, “Production and propagation of cosmic ray positrons and electrons,” *Astrophys. J.* **493**, 694–707 (1998).
88. E. Jourdain and J. P. Roques, “2003-2019 monitoring of the crab emission through INTEGRAL SPI, or vice versa,” *Astrophys. J.* **899**, 131 (2020).
89. S. Guiriec et al., “Gamma-ray science in the 2020s,” *Astro2020: Decadal Surv. Astron. Astrophys.* **2020**, 398 (2019).
90. Z. Wadiasingh et al., “Magnetars as astrophysical laboratories of extreme quantum electrodynamics: the case for a Compton telescope,” arXiv:1903.05648 (2019).
91. F. De Colle and W. Lu, “Jets from tidal disruption events,” *New Astron. Rev.* **89**, 101538 (2020).
92. M. Negro et al., “Unveiling the origin of the fermi bubbles with MeV photon telescopes,” *Astrophys. J.* **927**(2), 225 (2022).
93. K. Murase et al., “High-energy neutrino and gamma-ray emission from tidal disruption events,” *Astrophys. J.* **902**(2), 108 (2020).
94. H. Fleischhack, “AMEGO-X: MeV gamma-ray astronomy in the multi-messenger era,” in *PoS ICRC2021*, p. 649 (2021).
95. S. E. Boggs and P. Jean, “Event reconstruction in high resolution Compton telescopes,” *Astron. Astrophys. Suppl. Ser.* **145**, 311 (2000).
96. F. Lei, A. J. Dean, and G. L. Hills, “Compton polarimetry in gamma-ray astronomy,” *Space Sci. Rev.* **82**, 309–388 (1997).
97. A. Akyüz et al., “Enhanced performance of an electron tracking Compton gamma-ray telescope,” *New Astron.* **9**, 127–135 (2004).
98. W. B. Atwood et al., “The large area telescope on the fermi gamma-ray space telescope mission,” *Astrophys. J.* **697**, 1071–1102 (2009).
99. I. Martinez-Castellanos et al., “Improving the low-energy transient sensitivity of AMEGO-X using single-site events,” *Astrophys. J.* **934**, 92 (2021).
100. I. Brewer et al., “Developing the future of gamma-ray astrophysics with monolithic silicon pixels,” *Nucl. Instrum. Methods Phys. Res. Sect. A* **1019**, 165795 (2021).
101. I. Peric, “A novel monolithic pixelated particle detector implemented in high-voltage CMOS technology,” *Nucl. Instrum. Methods Phys. Res. Sect. A* **582**, 876–885 (2007).
102. I. Perić et al., “A high-voltage pixel sensor for the ATLAS upgrade,” *Nucl. Instrum. Methods Phys. Res. A* **924**, 99–103 (2019).
103. A. Schöning et al., “MuPix and ATLASPix – architectures and results,” in *PoS Vertex2019*, p. 024 (2020).
104. I. Peric et al., “High-voltage CMOS active pixel sensor,” *IEEE J. Solid State Circuits* **56**(8), 2488–2502 (2021).

105. R. Caputo et al., “AstroPix: investigating the potential of silicon pixel sensors in the future of gamma-ray astrophysics,” *Proc. SPIE* **11444**, 445–456 (2020).
106. D. Shy et al., “Development of dual-gain SIPMS to mitigate non-linearity,” in *IEEE Nucl. Sci. Symp. and Med. Imaging Conf. Proc. (NSS/MIC)*, pp. 1–6 (2021).
107. L. J. Mitchell et al., “Strontium iodide radiation instrumentation (SIRI),” *Proc. SPIE* **10397**, 103970B (2017).
108. L. J. Mitchell et al., “Radiation damage assessment of SensL SiPMs,” *Nucl. Instrum. Methods Phys. Res. A* **988**, 164798 (2021).
109. L. J. Mitchell et al., “Strontium iodide radiation instrument (SIRI) – early on-orbit results,” in *IEEE Nucl. Sci. Symp. and Med. Imaging Conf. (NSS/MIC)*, pp. 1–9 (2019).
110. R. S. Woolf et al., “Development of a CsI:Tl calorimeter subsystem for the all-sky medium-energy gamma-ray observatory (AMEGO),” in *IEEE Nucl. Sci. Symp. and Med. Imaging Conf. Proc. (NSS/MIC)*, pp. 1–6 (2018).
111. A. Zoglauer, R. Andritschke, and F. Schopper, “MEGAlib the medium energy gamma-ray astronomy library,” *New Astron. Rev.* **50**, 629–632 (2006).
112. S. Agostinelli et al., “Geant4—a simulation toolkit,” *Nucl. Instrum. and Methods Phys. Res. Sect. A* **506**(3), 250–303 (2003).
113. D. E. Gruber et al., “The spectrum of diffuse cosmic hard x-rays measured with HEAO-1,” *Astrophys. J.* **520**, 124 (1999).
114. G. Weidenspointner et al., “First identification and modelling of SPI background lines,” *Astron. Astrophys.* **411**, L113–L116 (2003).
115. T. Mizuno et al., “Cosmic-ray background flux model based on a gamma-ray large-area space telescope balloon flight engineering model,” *Astrophys. J.* **614**, 1113–1123 (2004).
116. R. Krivonos et al., “NuSTAR measurement of the cosmic X-ray background in the 3–20 keV energy band,” *Mon. Not. R. Astron. Soc.* **502**, 3966–3975 (2021).
117. P. Cumani et al., “Background for a gamma-ray satellite on a low-Earth orbit,” *Exp. Astron.* **47**(3), 273–302 (2019).
118. A. Zoglauer, “Using deep learning for the event reconstruction of combined Compton-scattering and pair-creation telescopes,” in *Am. Astron. Soc. Meeting Abstr.* **235**, 372.21 (2020).
119. M. Ackermann et al., “The fermi large area telescope on orbit: event classification, instrument response functions, and calibration,” *Astrophys. J. Suppl. Ser.* **203**, 4 (2012).
120. C. Meegan et al., “The fermi gamma-ray burst monitor,” *Astrophys. J.* **702**, 791–804 (2009).
121. W. S. Paciesas et al., “The fermi GBM gamma-ray burst catalog: the first two years,” *Astrophys. J. Suppl. Ser.* **199**, 18 (2012).
122. M. Wood et al., “Fermipy: an open-source Python package for analysis of Fermi-LAT Data,” in *35th Int. Cosmic Ray Conf. (ICRC2017)*, Vol. 301, p. 824 (2017).

Biographies of the authors are not available.